ADVANCED MATERIALS TECHNOLOGIES
www.advmattechnol.de

Full-Domain 3D Digital Twin for Comprehensive Analysis and Validation of Standing Surface Acoustic Wave Generation on $LiNbO_3$ Substrate

Felice Alberto Sfregola, Annalisa Volpe, Andrea Zifarelli, Massimiliano Benetti, Domenico Cannatà, Vincenzo Spagnolo, and Pietro Patimisco*

Standing Surface Acoustic Waves (SSAWs) generated on a piezoelectric substrate are largely used to create stable surface force patterns in active lab-on-a-chip devices. This study presents the development and experimental validation of a full-domain 3D digital twin for a SSAW device based on 128° YX $LiNbO_3$, commonly used for acoustofluidic applications. The model is developed in COMSOL Multiphysics to accurately capture the electromechanical interactions that govern SSAW generation and its interaction with the substrate. Its predictive accuracy is validated through electrical characterization with a vector network analyzer and surface displacement mapping with a laser Doppler vibrometer, demonstrating strong agreement between simulations and experimental data. This validation proves the reliability of digital twins for predictive modeling and design optimization of SSAW devices, offering a more precise and efficient alternative to traditional models and trial-and-error approaches.

1. Introduction

Surface acoustic wave (SAW) devices have seen significant advancements in recent years due to their ability to precisely manipulate surface acoustic energy, making them valuable in a wide range of applications.[1] Originally developed for telecommunications, where they play a critical role in high-frequency signal processing,[2] SAWs technology has expanded into fields such as mass detection and biochemical sensing.[3] This versatility has driven their integration into lab-on-a-chip (LOC) systems, enabling miniaturized diagnostics, including gravimetric detection and real-time biochemical analysis.[4] SAW technology has also found a role in quantum acoustodynamics, enabling strong interactions between surface waves and superconducting qubits, contributing to advancements in quantum computing.[5] In biomedical research, standing SAWs (SSAWs), specifically Rayleigh waves, enable precise, non-invasive manipulation of microparticles, cells, and fluids.[6] Early studies by Shi et al. demonstrated SSAWs as a powerful tool for particle manipulation,[7] continuous separation,[8] and precise cell patterning[9] in microfluidic channels, paving the way for acoustic tweezers and advanced particle sorting techniques. These innovations have enabled high-throughput SSAW-based cell sorting[10] and fluorescence-activated cell manipulation,[11] significantly enhancing the capabilities of microfluidic systems. Beyond cellular applications, SAW microfluidic platforms have been employed for extracellular vesicle enrichment,[12] offering promising breakthroughs in cancer biomarker discovery. As SSAW technology continues to evolve, accurate numerical modeling becomes essential for optimizing device performance and expanding its applicability. Developing high-fidelity digital twins capable of capturing complex electromechanical interactions is crucial to overcoming the limitations of traditional modeling approaches and accelerating the design and implementation of next-generation SSAW devices.

The physics governing SAW-based devices is inherently complex and involves the intricate coupling of multiple physical domains, including mechanics, piezoelectricity, acoustics, and fluid dynamics. Unlike simpler resonant systems, the interaction between acoustic waves and the surrounding medium cannot be solved analytically due to the nonlinear and anisotropic nature of the materials involved. Accurately capturing these effects requires advanced numerical models capable of resolving wave propagation and electromechanical coupling with high fidelity. Digital twins have emerged as an essential tool for optimizing

F. A. Sfregola, A. Volpe, A. Zifarelli, V. Spagnolo, P. Patimisco
Dipartimento Interateneo di Fisica
University and Politecnico of Bari
Via Amendola 173, Bari 70126, Italy
E-mail: annalisa.volpe@poliba.it
M. Benetti, D. Cannatà
Institute of Microelectronics and Microsystems
IMM-CNR
Via del Fosso del Cavaliere 100, Rome 00133, Italy
V. Spagnolo, P. Patimisco
PolySense Innovations srl
Via Amendola 173, Bari 70126, Italy

The ORCID identification number(s) for the author(s) of this article can be found under https://doi.org/10.1002/admt.202501275

DOI: 10.1002/admt.202501275

these devices, allowing for precise modeling of key SAW properties – including phase and group velocity, polarization, electromechanical coupling coefficient. In anisotropic substrates, these characteristics depend on the crystallographic plane and the wave propagation direction within the plane. Furthermore, when the Poynting vector and wave vector are not parallel, the power flow angle (PFA) is non-zero and causes beam steering,[13] making analytical solutions impossible and necessitating numerical modeling. The accuracy of a digital twin depends on rigorous validation against experimental data.[14] After their validation, digital twins enable precise prediction of system behavior under varying conditions, identification of optimal operating parameters, and acceleration of device design and testing. This approach not only reduces development costs and time but also overcomes the limitations of traditional trial-and-error methods, which often fail to account for the complex multiphysics interactions in SAW systems. For instance, in acoustofluidics, where SAWs interact with fluids and particles, an accurate numerical model is essential for predicting wave propagation, interference, and diffraction effects ultimately leading to improved device performance.

The characterization and optimization of SAW have traditionally relied on electrical measurements using a vector network analyzer (VNA), with limited adoption of experimental methods for directly measuring surface displacement and wave propagation.[15] However, electrical characterization alone provides a limited perspective, as it does not fully capture the intricate electromechanical interactions governing SAW systems behavior. Although some studies have combined experimental measurements with simulations, they have often relied on simplified computational domains. For example, Weser et al. analyzed the influence of interdigital transducer (IDT) parameters on SAW fields but limited their study to a reduced 2D computational domain, inherently neglecting critical 3D effects.[16] Similarly, Smagin et al. employed 3D simulations but simplified their models to reduced domains with a limited number of IDTs, which did not fully replicate experimental conditions.[17] Consequently, the predictive accuracy of these models remains uncertain, raising questions about their accuracy and applicability to real-world devices.

Given these limitations, the present work introduces a full-domain 3D digital twin of a 128° YX $LiNbO_3$ SSAW device, commonly used for SSAW generation in acoustophoresis applications. While 2D modeling remains attractive due to its reduced computational cost, it fails to capture essential 3D wave propagation effects, such as out-of-plane displacement components and the actual spatial distribution of acoustic energy. In contrast, a full 3D approach, though computationally intensive, enables a more accurate representation of the electromechanical coupling, wave interference, and device response under realistic operating conditions.

The digital twin was built in COMSOL Multiphysics to accurately simulate the generation, propagation, and interaction of SAWs on the actual device. The model was validated first through VNA characterization and subsequently with surface displacement measurements with an interferometer, enabling a direct and comprehensive comparison between the simulated and experimental frequency responses and displacement fields.

2. Background

Acoustic waves in piezoelectric materials arise from the intrinsic coupling between mechanical deformations and electrical polarization within the medium, known as piezoelectric effect. It is governed by a set of fundamental equations that describe how mechanical stress and strain interact with electric fields. The propagation of acoustic waves is described, in terms of displacement u, by the piezoelectric wave equation[18]

$$\rho \frac{\partial^2 u_i}{\partial t^2} = \sum_{j,k,l=1}^{3} c_{ijkl} \frac{\partial^2 u_k}{\partial x_j x_l} + \sum_{k=1}^{3} e_{ijk} \frac{\partial E_k}{\partial x_j} \tag{1}$$

where ρ is the material density, c_{ijkl} are the elastic stiffness coefficients, e_{ikj} are the piezoelectric constants, and $E_k = \partial\phi/\partial x_k$ represents the electric field components. The last term of the wave equation acts as a source for acoustic wave generation under a time-varying electrical potential. Piezoelectric materials are commonly used as efficient transducers, converting electrical signals into mechanical vibrations and vice versa. To have a unique solution for the system, Equation (1) must be coupled with continuity equation accounting for the principle of charge conservation within the material. The continuity equation can be expressed in terms of electric displacement D and charge density ρ_f as

$$\nabla \cdot D = \rho_f \tag{2}$$

In regions without free charges ($\rho_f = 0$), the electric displacement is solenoidal, and its divergence is zero.

SAWs are a specific solution of such a system in the form of elastic waves that propagate across the surface of a piezoelectric material with an amplitude that decays exponentially into the substrate. The strong coupling between electrical potential and SAWs has enabled various applications over the years, exploiting the interaction between surface deformation and the surrounding medium. These include the realization of sensing platforms for detecting gas or liquid species, as well as acoustophoresis in microfluidic devices. Among the various modes of SAW, Rayleigh waves are of particular interest due to their unique polarization characteristics and efficient surface confinement. Their elliptical particle motion enables strong coupling with surrounding medium, making them ideal, for example, for precise manipulation in microfluidic systems. The most used method for generating SAWs on piezoelectric substrates is through IDTs. They consist of periodic metallic electrodes (fingers) deposited onto the substrate surface, where an applied alternating voltage induces mechanical wave propagation via the inverse piezoelectric effect. The synchronism frequency of the IDT is determined by the relationship

$$f = \frac{v}{2p} \tag{3}$$

where v is the SAW velocity in the medium, and p is the finger periodicity. The frequency bandwidth of the IDT is a crucial parameter for the overall performance, particularly when SAW-based devices are used as oscillators.[19] It is influenced by parameters such as the electrode width, spacing, aperture, and is inversely proportional to the number of fingers in the IDT design.[1]

The efficiency of SAW excitation with IDTs depends on the choice of piezoelectric material, as well as the impedance matching between the IDT and the driving circuit. It is measured in terms of the electromechanical coupling coefficient K^2, which quantifies the ratio of mechanical energy converted in response to electrical input, and vice versa. For SAW devices, it is defined as[18]

$$K^2 = 2\frac{v_f - v_g}{v_f} \tag{4}$$

where v_f and v_g are the SAW phase velocities for free and electrically short-circuited surface, respectively. For anisotropic materials, such as $LiNbO_3$, the phase velocity depends on the crystal cut, and propagation direction, which also affects the coupling coefficient K^2. This directional dependence can lead to beam steering effects, where the energy of the travelling SAW propagates along a path dictated by the material's slowness curve rather than the initial wave vector direction.[15] As a result, optimizing IDT alignment with respect to the material's crystallographic axes is crucial for maximizing wave propagation efficiency and overall device performance.

SSAWs are generated when two counter-propagating SAWs interfere constructively, forming a periodic stationary wave pattern. This can be achieved by positioning two IDTs facing each other on a piezoelectric substrate, and exciting them simultaneously.[15] In acoustofluidics, SSAW devices have been utilized for manipulating microparticles[20] and biological cells[21] in LOC systems. The efficiency of SSAW-based particle manipulation is influenced by several parameters, including the applied frequency and wave amplitude.[22] Experimental studies using laser Doppler vibrometer (LDV) can provide insights into SSAW field distributions and validate theoretical models of particle transport mechanisms.

The electrical behavior of SAW devices is often analyzed using the modified Butterworth-Van Dyke (BVD) equivalent circuit model.[23] This model includes a motional branch with a series connection of resistance (R_m), inductance (L_m), and capacitance (C_m), representing energy losses, wave inertia, and mechanical compliance, respectively. Additionally, a static capacitance (C_0) is placed in parallel with this branch.[24] Although the BVD model offers a useful framework for analyzing SAW resonators, real-world devices involve complex interactions that cannot be completely captured by simplified lumped-element circuit models. Here, we propose 3D Finite Element Analysis (FEA) for modeling the full electromechanical behavior of SAW systems. FEA can enable a more accurate study of wave propagation and material anisotropy, addressing issues that analytical methods and equivalent circuit models fail to resolve.

3. Modeling

The model geometry reproduces the fabricated SSAW device to create a digital twin using COMSOL Multiphysics. The device consists of two identical opposing IDTs with a pitch of 200 µm and an aperture of 8500 µm, deposited on a 128° YX $LiNbO_3$ substrate with a thickness of 500 µm. A detailed description of the geometry and boundary conditions can be found in Supplementary File S1 (Supporting Information). The simulated structures include the full 3D device, as well as two reduced-domain models, consisting of a cross-sectional slice along the wave propagation direction, as shown in **Figure 1**. The reduced-domain models helps decrease the computational load without compromising accuracy in eigenfrequency analysis. Each domain is meshed to resolve the acoustic field while maintaining high computational efficiency.

The meshing strategy, including element types and resolution considerations, is discussed in Supplementary File S2 (Supporting Information). Convergence analysis confirmed that the optimal trade-off between numerical precision and efficiency is achieved with a maximum element size of $\lambda_{SAW}/6$.[25] A free-triangular surface mesh is applied to the substrate's top surface, while its depth is discretized using free-tetrahedral elements for the full 3D model (**Figure 2b**). In the reduced-domain models, a finer parametric sweep was implemented to enhance accuracy (Figure 2a). Material properties, including stiffness tensor, dielectric permittivity, and piezoelectric coefficients, were sourced from COMSOL's material library for 128° YX-cut $LiNbO_3$ and aluminum.

The simulation was conducted within a multi-physics framework combining solid mechanics and electrostatics modules. The solid mechanics module governs the elastic wave propagation, while the electrostatics module couples electric fields and mechanical strain using the constitutive piezoelectric relations.[18] To model the behavior of Rayleigh waves, a stress-free boundary condition was applied at the top surface of the substrate. At the bottom boundary, a vanishing field condition was imposed on both displacement u and electric potential ϕ, preventing wave reflections back into the domain. Additionally, low-reflective boundary conditions were applied at the edges of the domain to prevent reflections that could interfere with the standing wave pattern. Finally, in the reduced domain, periodic boundary conditions were imposed on the lateral edges to simulate an ideal infinite wavefront without any edge effects.

The first step in the simulation process is an eigenfrequency study to identify the natural oscillation modes (eigenmodes) of the device and determine the optimal frequency for Rayleigh wave excitation. The simulated frequency range was centered on the expected operating frequency of 19.5 MHz, as calculated using Equation (3), ensuring that 10 eigenmodes were identified within the reduced-domain model. These modes were analyzed based on the defining characteristics of Rayleigh-type SAWs, specifically by considering the ellipticity of surface displacement and its exponential decay into the substrate. It is important to note that modal analysis provides only qualitative insights into the mode shapes and does not yield quantitative information about displacement amplitudes, stress distribution, or electric potential, as no external loads are applied. The chosen selected eigenmode, identified at a frequency of 19.81 MHz, is shown in **Figure 3a** as a 3D plot of the displacement field for a single-wavelength unit domain.

Based on this result, a frequency-domain study was performed on the 3D full-model to simulate the device's electrical response over a frequency range matching the experimental characterization obtained using the VNA. The electrodes were excited with an AC voltage corresponding to the experimental drive conditions (i.e., $f_R = 19.47$ MHz, $V_{PP} = 4.2$ V), enabling the extraction of the numerical displacement field values along the same scan

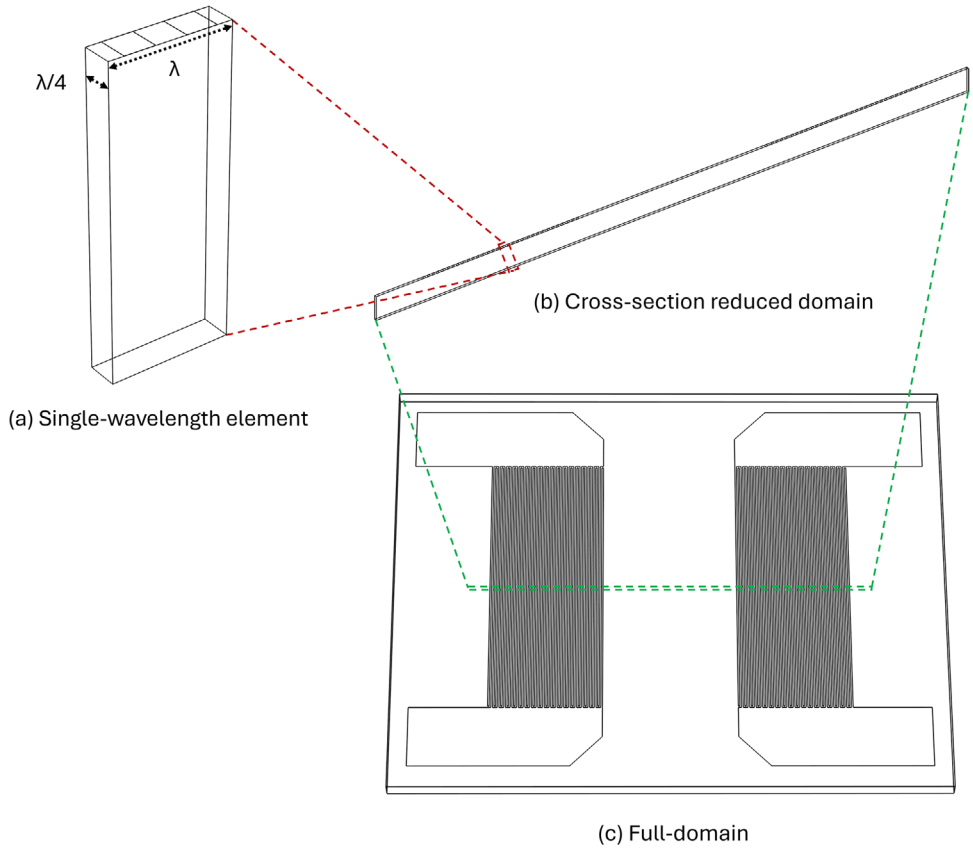

Figure 1. Schematic representation of the geometries used in simulations: a) single-wavelength element, b) reduced-domain model extracted from the full-domain cross-section, and c) full-domain model.

lines used in the displacement measurements. Figure 3b shows the simulated 3D standing displacement field along the normal direction to the surface, confirming the strong directionality of the SAW waves and the negligible impact of lateral bus bars. The computational time for the frequency sweep in the reduced-domain model was 6h 1min, while the full 3D model required 6h 40min, with the latter involving the solution of $\approx 2.3 \times 10^7$ degrees of freedom (DOFs). This demonstrates a reasonable computational cost despite the large problem size and highlights the scalability of the modeling approach.

Additionally, a time-domain analysis was conducted to examine the transient phase leading to the formation of a stable standing wave pattern. This study, which focuses on the first milliseconds of the system's dynamic response and the evolution of

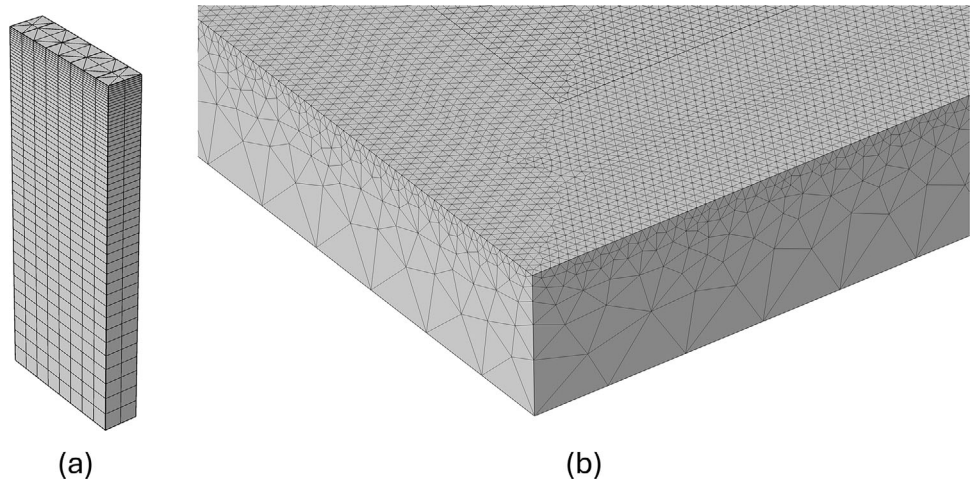

Figure 2. Mesh applied to a) reduced-domain models (single-wavelength element and cross-section) and b) full-domain model.

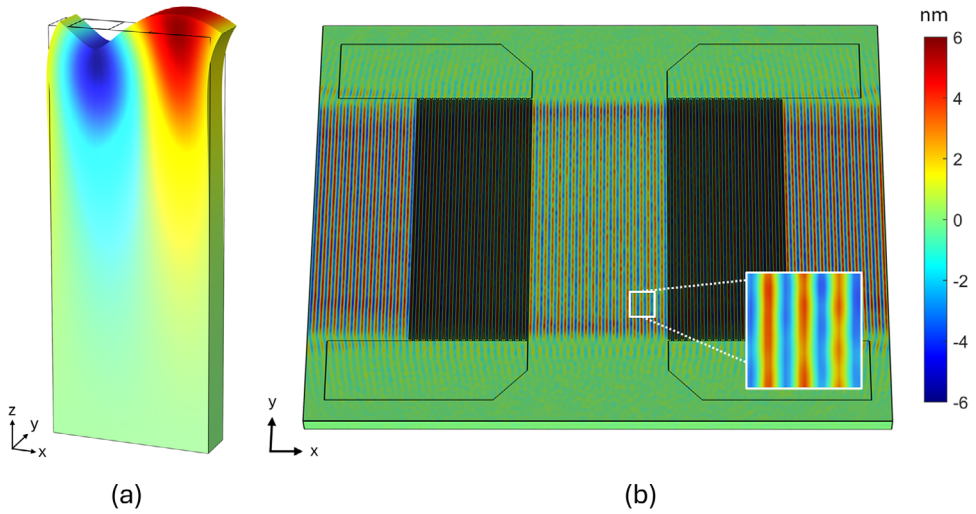

Figure 3. a) Out-of-plane displacement eigenmode for a single-wavelength element at the simulated resonance frequency of 19.81 MHz. The deformation is exaggerated for better visualization of the mode. b) Out-of-plane displacement for the full device under an AC signal corresponding to the experimental conditions (f_R = 19.44 MHz, V_{PP} = 4.2 V). The inset provides a magnified view of alternating nodal and antinodal lines.

wave interference, is detailed in the Supplementary File S3 (Supporting Information). Finally, the simulation was repeated with one IDT grounded to investigate the impact of IDT passivation on SAW field generation. These numerical simulations provide a direct comparison with the measurements that will be presented in the next section.

4. Results and Discussion

4.1. Device Electromechanical Characterization

The electrical response of the device was evaluated within over a 4 MHz range, with a 100-Hz bandwidth, centered at the expected operating frequency of 19.5 MHz (see Section 6). **Figures** 4a and 3b display the real and imaginary components of admittance, respectively, with both experimental and simulated data normalized to their respective peak values. The good agreement between the two datasets confirms the accuracy of the model, particularly in predicting the resonance peak at 19.47 MHz. This highlights the advantages of FEA in providing a highly accurate representation of real 3D systems, capturing complex electromechanical interactions that cannot be fully described using analytical models.

The mechanical response of the SSAW device was first characterized by measuring the displacement amplitude on an antinode point of the SSAW pattern at different excitation frequencies (see Section 6), as shown in **Figure 5**. The highest resonance peak was observed at 19.44 MHz, with a bandwidth of 100 kHz.

The frequency response peaks at 19.47 and 19.44 MHz, obtained through electrical and mechanical characterization, respectively, show excellent agreement. This validates the strong electromechanical coupling of the device and justify the widespread use of the Butterworth-Van Dyke equivalent circuit of SSAW devices, where mechanical elements are modeled as a series of lumped electrical components dependent on the device's physical properties.

The mechanical behavior of the SSAW device was further examined by measuring the displacement amplitude on an antinode point as a function of peak-to-peak excitation voltage at 19.44 MHz, which maximizes the out-of-plane displacement at an antinode point. The reconstructed characteristic curve in **Figure 6** shows a linear region between 0.5 and 5 V, with an

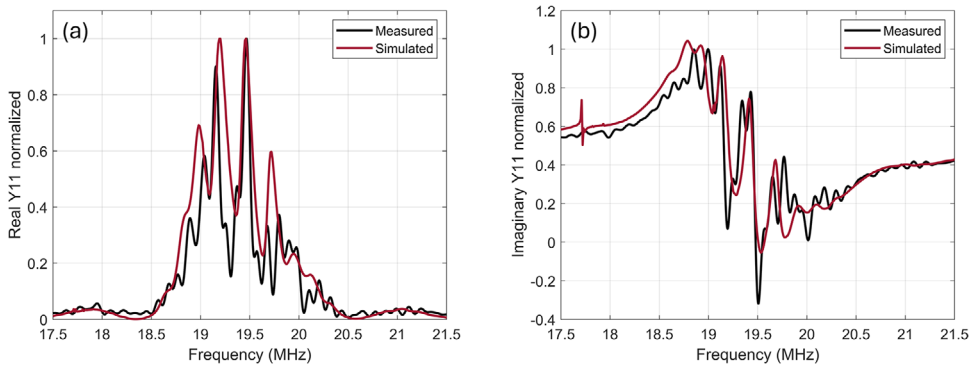

Figure 4. a) Real and b) imaginary parts of the measured (black) and simulated (red) admittance.

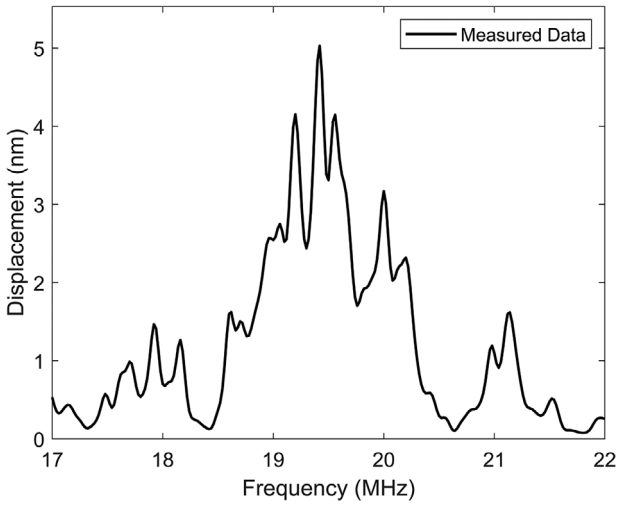

Figure 5. Out-of-plane displacement measured at an antinode as a function of the excitation frequency.

efficiency of 1.29 nm V^{-1}. Beyond this range, a deviation from linearity was observed, likely due to polarization saturation effects as the electric field approaches the material's breakdown threshold.[26] Hereafter, the driving voltage was fixed to 4.2 V to guarantee a linear response of the device while achieving a strong displacement amplitude.

4.2. SSAW Displacement Field Mapping

The surface displacement field within the IDTs active region was mapped using an LDV with a 14 µm spot size, capable of resolving out-of-plane displacements with sub-nanometer precision. As shown in **Figure 7**, the experimental setup (see Section 6) employed a waveform generator generating a sinusoidal signal

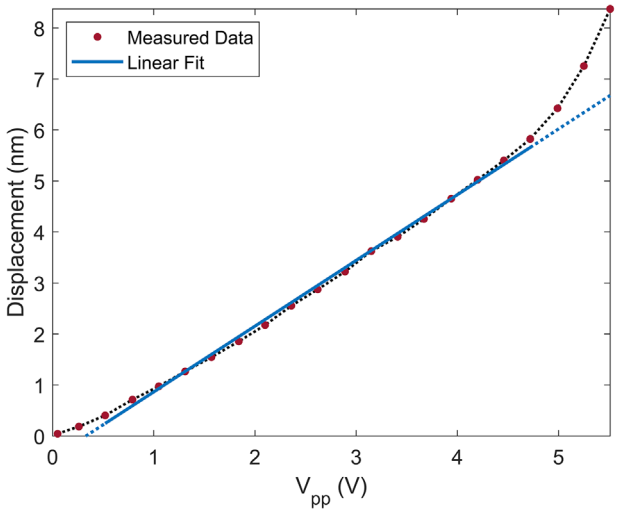

Figure 6. Out-of-plane displacement measured at an antinode as a function of the peak-to-peak voltage V_{pp} at f_r = 19.44 MHz. The solid blue line represents the linear fit in the region where the device response is linear, while the dashed line extends beyond this region to illustrate deviations from linearity.

that was amplified and split to simultaneously drive both IDTs, generating SSAWs. The LDV beam was aligned perpendicular to the device surface and focused using a three-axis micro-translator system.

The measurement procedure (see Section 6) involved systematically scanning the LDV beam across the active region while maintaining excitation at the device's resonance frequency f_r with a constant peak-to-peak driving voltage (V_{pp} = 4.2 V). This approach enabled 2D comprehensive characterization of the SSAW displacement field with a spatial resolution of 20 µm.

The first scanning line (orange dashed line in Figure 7) follows the wave propagation direction, from one IDT to the other. The raw displacement measurement in **Figure 8a** reveals a periodic pattern with regularly spaced peaks with an average amplitude of 4.23 µm. Due to the interferometric nature of the LDV acquisition, the measured output corresponds to the absolute oscillation amplitude at each scanned point. Consequently, peaks resemble the perfect alternation of node and antinode points. However, variations in the recorded peak-to-peak amplitude suggest the presence of additional spectral components in the measured signal.

To identify and analyze these unwanted spectral components, a Fourier transform algorithm was applied to the displacement data. As shown in Figure 8b, the resulting spectrum reveals a dominant component at 102.8 µm (k = 0.062 rad μm^{-1}), corresponding to half of the Rayleigh wavelength, an artifact of the measurement method, as previously discussed. The presence of lower-frequency components below 0.05 rad μm^{-1}, which cause variations in peaks amplitudes, can be attributed to wave reflections at both the device boundaries and the IDT structures.[27] **Figure 9a** shows the reconstructed pattern after applying a high-pass filter with a cutoff frequency of 0.05 rad/µm, effectively removing these low-frequency contributions.

A direct comparison with simulation data (Figure 9b) shows a strong correlation between the measured and simulated displacement values, with a cross-correlation coefficient of 0.925 and a perfect match in the number of peaks. However, certain limitations of the LDV measurements should be considered when interpreting the displacement values on y-axis. The laser spot, acting as a probe of the displacement field, is not a point source but rather has a gaussian-like profile with an FWHM of 14 µm. Consequently, each measurement point can be viewed as the result of an integration of the laser intensity distribution across the illuminated area. This characteristic of the measurement method explains why, even after band-pass filtering, slight discrepancies persist between the measured and theoretical displacement values, and why nodal points are not detected as exact zero-displacement values.

The second scanning line was taken perpendicular to wave propagation, at the midpoint between the two IDTs, following an antinode line (green dashed line in Figure 7). **Figure 10.** presents a comparative plot of the simulated and measured displacement mappings, demonstrating a strong overlap between the two datasets. Both trends exhibit a central plateau-like region, flanked by two small lateral lobes corresponding to slightly higher displacement amplitudes, which are more pronounced in the experimental dataset. This discrepancy can be attributed to wave diffraction effects, as both IDTs act as a finite aperture with dimensions comparable to the SAW wavelength.[27,28]

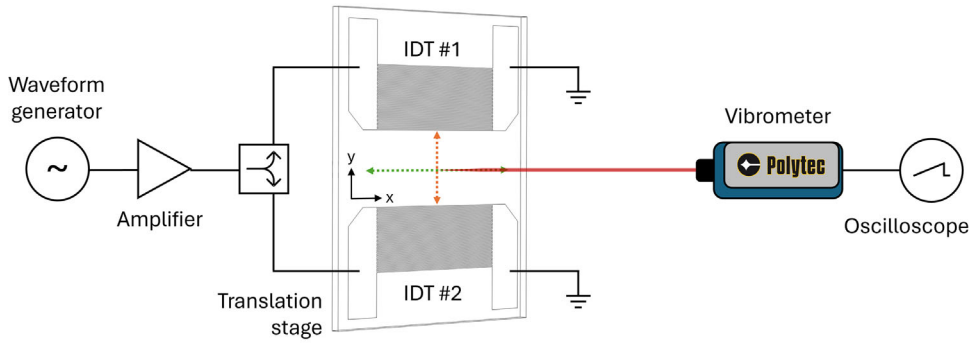

Figure 7. Schematic representation of the experimental setup for SSAW field mapping. The scanning lines for mapping are indicated with orange and green dashed arrows, corresponding to the directions parallel and perpendicular to the wave propagation, respectively.

Finally, measurements were also performed by exciting only one IDT while grounding the other to study wave propagation in a single-IDT configuration and its impact on the second one. Following the same analysis performed for dual-IDT excitation for SSAW generation, **Figure 11** presents a comprehensive comparison of the results: the raw displacement data (Figure 11a) compared with the SSAW case (Figure 8a); the trend after applying the Fourier transform algorithm (Figure 11b comparable to Figure 8b); reconstructed wave profile after applying a high-pass filter (Figure 11c comparable to Figure 9a); simulated displacement field (Figure 11d comparable to the dual-IDT simulation in Figure 9b).

The low-frequency spectral components below 0.05 rad μm^{-1} in Figure 11b demonstrate the absence of counter-propagating waves in this configuration, leading to a more uniform displacement field with negligible peak-to-peak variations caused by interference effects (Figure 11c,d). Also, a direct comparison between Figures 9b and 11d demonstrates the ability of the 3D full-domain digital twin to account for wave reflections from one IDT

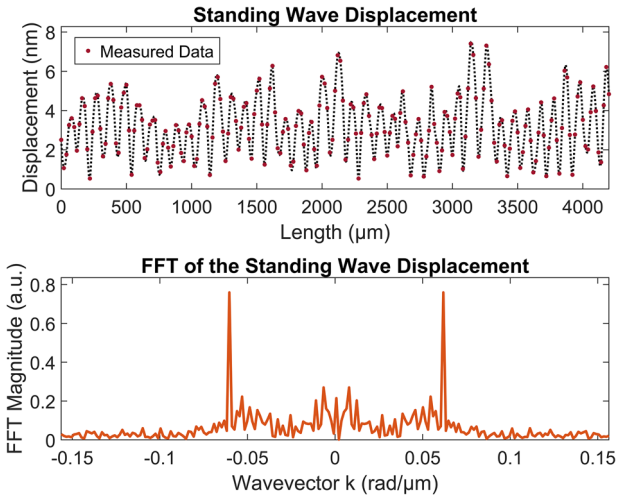

Figure 8. a) Out-of-plane displacement measured along the SAW propagation direction. The error on each data point is 0.47 nm and it was evaluated as the average mean absolute deviation across the repeated scans. The black dashed line serves as a visual guide. b) FFT of the measured displacement plotted in the wavevector space.

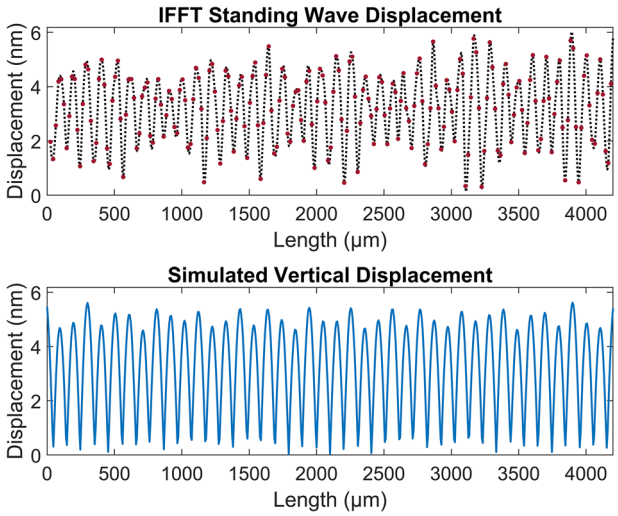

Figure 9. a) Out-of-plane displacement reconstructed through IFFT after suppressing low-frequency components. The black dashed line serves as a visual guide. b) Simulated out-of-plane displacement along the SAW propagation direction.

to the other in the simulation. Finally, the average oscillation amplitude for SAW propagation (single-IDT excitation, Figure 11a) is 2.92 μm, ≈70% of that observed in the SSAW configuration (dual-IDT excitation, Figure 8a). This result confirms that the number of active IDTs directly affects wave generation efficiency and highlights the critical role of transducer configuration in optimizing device performance.

5. Conclusion

This study presented the modeling, simulation, and experimental validation of a SSAW-based device for Rayleigh-type standing wave generation. A digital twin was developed using COMSOL Multiphysics to predict both the electrical and mechanical response of the system. The frequency domain study effectively replicated the experimental conditions, providing valuable insights into the system's electromechanical coupling and wave propagation characteristics. The experimental validation was conducted through LDV, which allowed precise measurement of the out-of-plane displacement field with nanometric

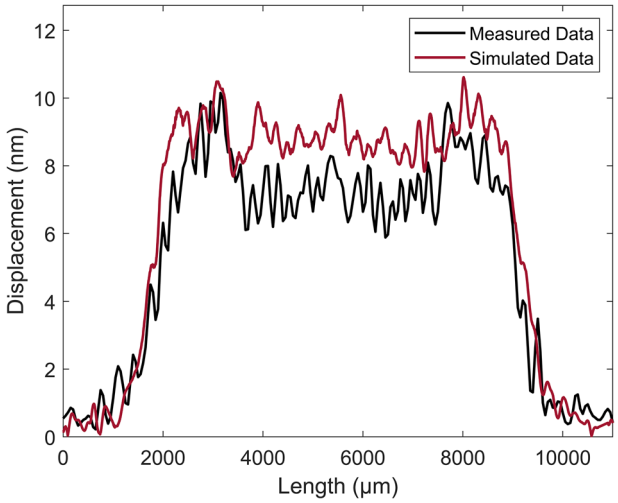

Figure 10. Out-of-plane displacement measured (black) and simulated (red) along an antinode scan line.

resolution. This methodology facilitated a direct comparison between the simulated and observed wave behavior, further reinforcing the reliability of the FEA model. Compared to other modeling approaches, such as the modified BVD equivalent circuit, FEA has proved to offer a more comprehensive representation of the physical phenomena. It not only predicted physical quantities with high accuracy but also captured wave propagation effects such as interference and diffraction, resulting in a more accurate and predictive model of the overall SAW device performance.

By demonstrating strong agreement between simulation and experiment, this study lays the foundation for advanced simulations that integrate more complex systems, such as microfluidic channels where the interaction between acoustic waves and fluid flows must also be modeled. In this context, 3D full-domain digital twins will drive the design of optimized acoustofluidic devices for several applications, like particle manipulation, droplet control, and enhanced biosensing in LOC systems. These modeling techniques will provide a systematic framework for analyzing surface waves-fluids interactions and the resulting acoustic force fields, which influence particle motion based on factors like size, density, and compressibility. This shift toward simulation-driven design will drive the next generation of high-performance SAW-based microfluidic devices, speeding up their adoption in biomedical and industrial applications.

6. Experimental Section

Materials: The SSAW-based device was fabricated using 128° YX-cut lithium niobate ($LiNbO_3$), widely recognized for its high electromechanical coupling coefficient and low acoustic losses. Specifically, this crystal orientation provides enhanced wave propagation speed (≈ 3980 m s^{-1} for Rayleigh waves) and a coupling coefficient K^2 of ≈5.5%, significantly higher than alternative materials such as quartz (0.16%), zinc oxide (1.1%), or aluminum nitride (0.4%).[29,30] Additionally, its Curie temperature of ≈1210 °C ensures thermal stability, making it highly reliable for long-term stability.

Device Fabrication: The IDTs were patterned onto the $LiNbO_3$ substrate by conventional photolithographic process using negative photoresist, exposed by UV radiation (Mask Aligner EVG 610). The metallic film was made of Al (thickness 200 nm) grown by radio frequency magnetron sputtering from a 99.999 % pure Al target in an Ar (99.999 % pure) atmosphere. Finally, a lift-off procedure allows to remove the unexposed resist in order to obtain the electrodes geometry. Key parameters such as the number of electrode pairs, aperture width, and periodicity are listed in **Table 1**.

Experimental Setup: The experimental setup consists of a waveform generator (Model SMB100B, Rohde&Schwarz GmbH) connected to a broadband amplifier (Model BBA150, Rohde & Schwarz GmbH), which excites both IDTs simultaneously with a sinusoidal waveform using a power splitter, as schematized in Figure 7. A VNA (Model ZNL3, Rohde & Schwarz GmbH) was used to assess the device's frequency response and impedance characteristics as part of its electrical characterization. A laser doppler vibrometer (LDV, Model VFX-F-110, Polytec GmbH) was used to detect out-of-plane displacements caused by SSAWs generated when both IDTs are excited.

For the interferometric measurements, the sample was mounted on a mechanical three-axis micro-translator. The beam of the LDV was aligned perpendicularly to the device surface and focused on it with a spot size of 14 μm on the surface. The LDV was configured to detect vibrations up to 24 MHz, applying a high-pass filter to remove low-frequency mechanical oscillations below 60 kHz. This configuration allowed for the detection of displacements with amplitudes below one nanometer. An oscilloscope was used to visualize and store the LDV signal for post-processing analysis.

Methods: The scanning strategy followed a systematic approach to ensure high measurement accuracy and repeatability. First, the contribution of electronic noise was evaluated, and the temporal stability of the device

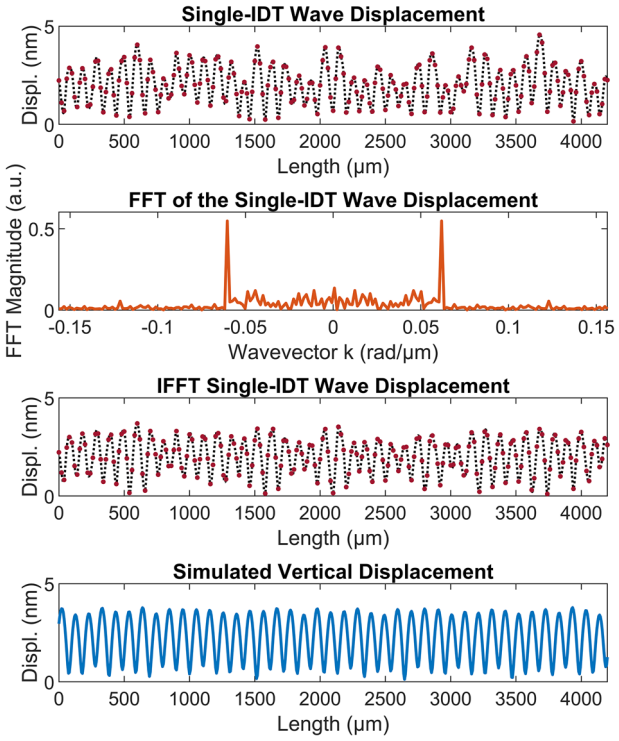

Figure 11. a) Out-of-plane displacement measured along the SAW propagation direction in the single-IDT configuration. The error on each data point is 0.07 nm and it was evaluated as the average mean absolute deviation across the repeated scans. The black dashed line serves as a visual guide. b) FFT of the measured displacement plotted in wavevector space. c) Out-of-plane reconstructed displacement using IFFT after suppressing low-frequency components. d) Out-of-plane displacement simulated along the SAW propagation direction in the single-IDT configuration.

Table 1. Key design parameters of the IDTs fabricated on the $LiNbO_3$ substrate.

Periodicity (p) [μm]	Number of electrode pairs (N_c)	Aperture width (W) [μm]	Centre-to-Centre distance [μm]	Al thickness [μm]
100	18	8500	7750	0.15

response was verified to exclude hysteresis effects. The LDV beam was then focused on a selected antinode point of the standing wave pattern generated by the SSAW to record out-of-plane displacement values, both at different excitation frequencies and peak-to-peak voltage levels. The resonance frequency f_R was identified as the value at which the displacement amplitude reaches its maximum. Additionally, the linear response range as a function of the sinusoidal voltage V_{PP} applied to both IDTs was determined. The full mapping of the surface displacement pattern was performed at the resonance frequency and fixed driving voltage. Measurements were acquired with a spatial resolution of 20 μm, corresponding to at least 10 data points per wavelength. The surface mapping was performed along both directions, parallel and perpendicular to the wave propagation, as indicated in Figure 7. Each scan was repeated three times to improve statistical reliability and minimize measurement uncertainty.

The SAW propagation behavior was further investigated by selectively exciting one IDT while grounding the other. This configuration enabled a direct comparison between the double-IDT excitation, which generates SSAWs, and single-IDT excitation, which produces traveling SAWs. The collected measurements were processed using a Fourier transform-based algorithm to analyze the frequency components of the temporal signal acquired by LDV.

Supporting Information

Supporting Information is available from the Wiley Online Library or from the author.

Acknowledgements

This work was supported by MUR in the framework of the PRIN 2022 PNRR Project "Surface and Interface acoustic wave-driven Microfluidic devices-BAsed on fs-laser technology for particle sorting (SIMBA)" (Grant No. Prot. P2022LMRKB) and the project "Quantum Sensing and Modeling for One-Health (QuaSiModO)" (CUP: H97G23000100001).

Conflict of Interest

The authors declare no conflict of interest.

Author Contributions

F.A.S. performed the conceptualization, investigation, formal analysis, visualization, and wrote the original draft; A.V. contributed to the writing, reviewing and editing, and supervision. Andrea Zifarelli contributed to the investigation, visualization, and wrote, reviewed, and edited the manuscript; M.B. contributed to the investigation, formal analysis and wrote, reviewed, and edited the manuscript; D.C. contributed to the investigation and wrote, reviewed, and edited the manuscript; V.S. contributed to formal analysis and wrote, reviewed, and edited the manuscript; P.P. was responsible for the conceptualization, formal analysis, visualization, writing – review and editing, and supervision.

Data Availability Statement

The data that support the findings of this study are available from the corresponding author upon reasonable request.

Keywords

digital twin, finite element analysis, MEMS, microfluidics, surface acoustic waves

Received: July 30, 2025
Revised: August 27, 2025
Published online: September 19, 2025

[1] D. Mandal, S. Banerjee, *Sensors* **2022**, *22*, 820.
[2] R. M. Hays, C. S. Hartmann, *Proceedings of the IEEE* **1976**, *64*, 652.
[3] D. B. Go, M. Z. Atashbar, Z. Ramshani, H. C. Chang, *Anal. Methods* **2017**, *9*, 4112.
[4] J. Qian, Y. Wang, Y. Xue, H. Begum, Y. Q. Fu, J. E. Y. Lee, *Appl. Phys. Rev.* **2025**, *12*, 11401.
[5] R. Manenti, A. F. Kockum, A. Patterson, T. Behrle, J. Rahamim, G. Tancredi, F. Nori, P. J. Leek, *Nat. Commun.* **2017**, *8*, 975.
[6] J. Friend, L. Y. Yeo, *Rev. Mod. Phys.* **2011**, *83*, 647.
[7] J. Shi, X. Mao, D. Ahmed, A. Colletti, T. J. Huang, *Lab Chip* **2008**, *8*, 221.
[8] J. Shi, H. Huang, Z. Stratton, Y. Huang, T. J. Huang, *Lab Chip* **2009**, *9*, 3354.
[9] J. Shi, D. Ahmed, X. Mao, S. C. S. Lin, A. Lawit, T. J. Huang, *Lab Chip* **2009**, *9*, 2890.
[10] S. Li, X. Ding, Z. Mao, Y. Chen, N. Nama, F. Guo, P. Li, L. Wang, C. E. Cameron, T. J. Huang, *Lab Chip* **2014**, *15*, 331.
[11] L. Ren, S. Yang, P. Zhang, Z. Qu, Z. Mao, P. H. Huang, Y. Chen, M. Wu, L. Wang, P. Li, T. J. Huang, *Small* **2018**, *14*, http://10.1002/SMLL.201801996.
[12] A. Ku, H. C. Lim, M. Evander, H. Lilja, T. Laurell, S. Scheding, Y. Ceder, *Anal. Chem.* **2018**, *90*, 8011.
[13] I. E. Kuznetsova, B. D. Zaitsev, A. A. Teplykh, S. G. Joshi, A. S. Kuznetsova, *IEEE Trans. Ultrason. Ferroelectr. Freq. Control* **2008**, *55*, 1984.
[14] A. Volpe, P. Paiè, A. Ancona, R. Osellame, P. M. Lugarà, G. Pascazio, *J. Phys. D: Appl. Phys.* **2017**, *50*, 255601.
[15] R. Weser, A. Winkler, M. Weihnacht, S. Menzel, H. Schmidt, *Ultrasonics* **2020**, *106*, 106160.
[16] R. Weser, A. N. Darinskii, M. Weihnacht, H. Schmidt, *Ultrasonics* **2020**, *106*, 106077.
[17] N. Smagin, L. Djoumi, E. Herth, M. Vanotti, D. Fall, V. Blondeau-Patissier, M. Duquennoy, M. Ouaftouh, *Sens. Actuators A Phys.* **2017**, *264*, 96.
[18] D. S. Ballantine, S. J. Martin, A. J. Ricco, G. C. Frye, H. Wohltjen, R. M. White, E. T. Zellers, *Acoustic Wave Sensors* **1997**, 10.
[19] D. S. Ballantine, S. J. Martin, A. J. Ricco, G. C. Frye, H. Wohltjen, R. M. White, E. T. Zellers, *Acoustic Wave Sensors* **1997**, 36.
[20] J. Shi, S. Yazdi, S. C. Steven Lin, X. Ding, I. K. Chiang, K. Sharp, T. J. Huang, *Lab Chip* **2011**, *11*, 2319.
[21] M. Dao, S. Suresh, T. J. Huang, P. Li, Z. Mao, Z. Peng, L. Zhou, Y. Chen, P. H. Huang, C. I. Truica, J. J. Drabick, W. S. El-Deiry, *Proc. Natl. Acad. Sci. USA* **2015**, *112*, 4970.
[22] D. Hartono, Y. Liu, P. L. Tan, X. Y. S. Then, L. Y. L. Yung, K. M. Lim, *Lab Chip* **2011**, *11*, 4072.

[23] T. E. Parker, G. K. Montress, *IEEE Trans. Ultrason. Ferroelectr. Freq. Control* **1988**, *35*, 342.
[24] D. Neculoiu, A. C. Bunea, A. M. Dinescu, L. A. Farhat, *IEEE Access* **2018**, *6*, 47587.
[25] J. Lei, P. Glynne-Jones, M. Hill, *Lab Chip* **2013**, *13*, 2133.
[26] F. S. Hickernell, P. L. Clar, I. R. Cook, in *1972 Ultrasonics Symposium*, IEEE, Boston, MA, USA **1972**.
[27] Y. Zhang, J. Huang, X. Guo, *J. Micromech. Microeng.* **2021**, *31*, 094001.
[28] A. Fakhfouri, C. Devendran, T. Albrecht, D. J. Collins, A. Winkler, H. Schmidt, A. Neild, *Lab Chip* **2018**, *18*, 2214.
[29] W.-K. Tseng, J.-L. Lin, W.-C. Sung, S.-H. Chen, G.-B. Lee, *J. Micromech. Microeng.* **2006**, *16*, 539.
[30] F. A. Sfregola, R. De Palo, C. Gaudiuso, F. P. Mezzapesa, P. Patimisco, A. Ancona, A. Volpe, *Opt. Laser Technol.* **2024**, *177*, 111067.